AUT Journal of Electrical Engineering
10.22060/EEJ.2025.23756.5632

Vertical Tunneling Transistor Based on Gr-hBN-χ_3 Borophene Heterostructure with AA Stack

Reza Abbasi,[1]* Rahim Faez,[2] Ashkan Horri [3]

[1] Department of Electrical and Computer Engineering, Science and Research Branch, Islamic Azad University, Tehran, 1477893855, Iran
[2] Department of Electrical Engineering, Sharif University of Technology, Tehran, 1458889694, Iran
[3] Department of Electrical Engineering, Arak Branch, Islamic Azad University, Arak, 3836119131, Iran

ABSTRACT

In this paper, the electronic properties of vertical Gr-hBN-χ_3 borophene heterostructure (AA stack between Gr and hBN layers), i.e. (Gr-hBN-χ_3_AA), have been investigated by density functional theory (DFT). By using the tight-binding (TB) model and least-square fitting for TB and DFT band structures, optimal TB parameters are calculated. By exploiting the non-equilibrium Green function technique and capacitive model, we have investigated the vertical tunneling transistor (VTFET) based on Gr-hBN-χ_3_AA. Also, the figure of merit (FOM) of the device, such as the I_{ON}/I_{OFF} ratio, subthreshold swing, and intrinsic gate-delay time, have been extracted. We have concluded that decreasing the width of graphene nanoribbon improves the switching ratio, subthreshold swing, and gate-delay time. Also, compared to previous work (VTFET based on Gr-hBN-χ_3_AB), it is seen that changing the stack between Gr and hBN layers has little effect on the FOM of the device. The gate-delay time of the device is 0.011 ps at room temperature.

Keywords: Borophene, Density functional theory, Nonequilibrium Green function, Vertical tunneling transistor

1. Introduction

The fast growth of information technology (IT) has been sustained by the continuous scaling down of the transistors dimensions. In the last decade, on the one hand, two-dimensional (2D) [1], transition-metal-dichalcogenides (TMD) [2], and metallic-transition-metal-dichalcogenides (MTMDs) [3] and on the other hand innovative structures [4], have played an important role in this regard. One of these innovative structures is vertical heterostructure. Vertical structures with van der Walls (vdW) bonds between layers are promising to reduce the size and energy consumption of the device and keep Moore's law stable [5-8]. However, those suffering from a lattice mismatch and displacement of layers [9]. Nevertheless, IBM and SAMSUNG companies have introduced new vertical tunneling transistor (VTFET) to help sustain Moore's law for years to come [10].

In 2012, the first VTFET based on Gr-hBN(MoS_2)-Gr heterostructures was proposed and fabricated [11]. In the last decade, VTFETs based on Gr-hBCN [12], Gr-TMD [13], II-type heterostructure [14], and 3D-2D heterostructures [15] have been investigated. Also, VTFETs with metallic drain have been presented as follows. In 2013, Yu et al. experimentally investigated a VTFET based on Gr-MoS_2-Ti heterostructure [16]. In 2021, Lee et al. [17] (Liu et al. [18]) reported a VTFET based on Gr-hBN-metal (Gr-MoS_2-Ag) heterostructure. In 2022, Abbasi et al. theoretically proposed and investigated another VTFET based on Gr-

[1] Corresponding author email: reza.abbasi@srbiau.ac.ir
[2] faez@sharif.edu
[3] a-horri@iau-arak.ac.ir

10.22060/EEJ.2025.23756.5632
hBN-χ_3 borophene heterostructure [19]. However, VTFETs have the potential to be designed and fabricated with sub-1-nm gate length [20].

In this work, we numerically simulate a tunneling transistor based on vertical Gr-hBN-χ_3 borophene heterostructure (AA stack between Gr and hBN layers), i.e. (Gr-hBN-χ_3_AA). We have investigated the effect of changing the stack between Gr and hBN layers compared to reference [19].

Borophene is a 2D material with different phases that was first realized on the silver crystal substrate by the MBE system [21, 22]. This material has unique physical, chemical, and optical properties and could be a candidate for the next generation of electronics [23-26]. However, so far, its instability has limited its large-scale applications. Meanwhile, the three main structures of borophene are χ_3, β_{12}, and striped borophene [21, 22]; also, new phases of borophene, such as the glass state of borophene, liquid borophene, and borophene with large holes have been discovered [27]. The χ_3 borophene has metallic properties [28], and in this work, it has been used in the drain of the device.

We exploited the non-equilibrium Green Function (NEGF) formalism combined with the tight-binding (TB) and capacitive models to calculate the electrical characteristics of VTGrχ_3FET (AA stack between Gr and hBN layers). The article's organization is as follows: Section 2 describes the energy band diagram of the device. The first-principle results, TB model, and NEGF are presented in Section 3. Section 4 discusses the results. Finally, the conclusion is expressed in 5.

2. Device structure and Operational principle

Fig. 1 shows the apparent schematic of the device with two contacts. Fig. 2(a) presents a cross-sectional view of the physical structure and band alignment of the device. The source (drain) in the device is graphene (χ_3 borophene). Those are electrically separated by one layer of hBN barrier. The gate oxide is SiO_2, and a layer of hBN is exfoliated on it [11]. The stack type between graphene and hBN layers is assumed AA. Fig. 2(b) illustrates the band diagram of the VTGrχ_3FET in zero bias. For $V_{GS} < 0$, the Fermi level shifts downwards, reducing the effective height of the tunneling barrier, which represents the ON state (Fig. 2(c)), whilst the Fermi level shifts upwards by applying a $V_{GS} > 0$, therefore the effective height of the tunneling barrier increases, which shows the OFF state In Fig. 2(d). The voltage between the graphene and χ_3 borophene sheets (V_B) controls the tunneling current. This structure uses graphene's low density of states (DOS) feature. As shown in Fig. 2, the DOS of graphene and χ_3 borophene and the effective height of the barriers are modified by varying the gate-source voltage. Hence, the current is modulated. The device's manufacturing process can be similar VTFET based on Gr-hBN-Gr heterostructure [11].

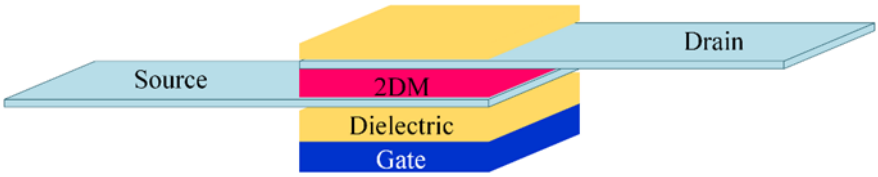

Fig.1. Apparent schematic of the device.

10.22060/EEJ.2025.23756.5632

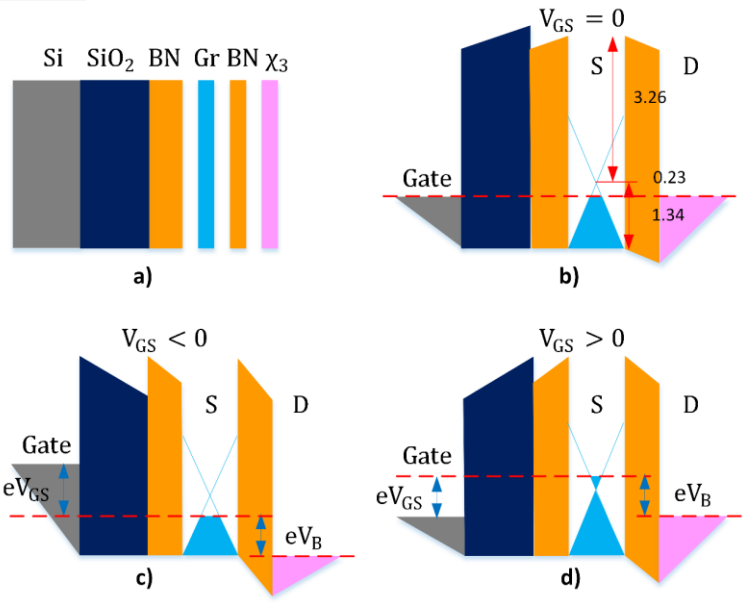

Fig. 2. (a) Schematic of VTGrχ_3FET. Band diagram corresponding to (b) No bias, (c) ON state, and (d) OFF state.

3. Band Structure and Modeling

A. First principle calculation

To discover the electronic properties of Gr-hBN-χ_3_AA vertical heterostructure, we have exploited the density functional theory (DFT). DFT calculations are carried out by quantum espresso (QE) software [29]. In the process of relaxation, the structure is relaxed until the forces acting on atoms become smaller than 10^{-2} Ry/Bohr. After geometric optimization, the calculated interlayer distance between the Gr and hBN (hBN and χ_3 borophene) is 4.07 (4.18) Å. To eliminate the interactions between supercell images, a vacuum spacing of 17 Å has been adopted along the perpendicular direction to the structure (z). The generalized gradient approximation (GGA) of Perdew–Burke–Ernzerhof (PBE) is selected to approximate the electronic exchange and correlation. The cut-off energy of the wave function (charge density) is 70 (280) Ry. Also, numerical integrations in the Brillon zone is evaluated with the Monkhorst-Pack mesh (14 × 8 × 1).

Fig. 3 shows the geometry of the Gr-hBN-χ_3_AA vertical heterostructure after the relaxation process. In supercell, the number of boron, carbon, and nitrogen atoms is 64, 48, and 24, respectively. We calculated the binding energy of heterostructure as $E_b = \left[E_{HS} - E_{Gr} - E_{hBN} - E_{\chi_3}\right]$ to investigate the stability of the structure. In this formula, E_{HS}, E_{Gr}, E_{hBN}, and E_{χ_3} are the total energy of the heterostructure, isolated layered Gr, hBN, and χ_3 borophene, respectively. The binding energy for supercell is – 0.0945 eV. This negative value means that the structure is stable. This parameter for Gr-hBN-χ_3_AB (AB stack between Gr and hBN) is – 0.1244 eV [19]; therefore, Gr-hBN-χ_3_AA is less stable than Gr-hBN-χ_3_AB. An important parameter in vertical heterostructures is lattice mismatch [9]. The lattice mismatch between hBN and χ_3 borophene layers is calculated at 0.0366 (0.0373) in the X (Y) directions for Gr-hBN-χ_3_AA vertical heterostructure. Since these values are small, they have little effect on the electronic characteristics of the structure.

10.22060/EEJ.2025.23756.5632

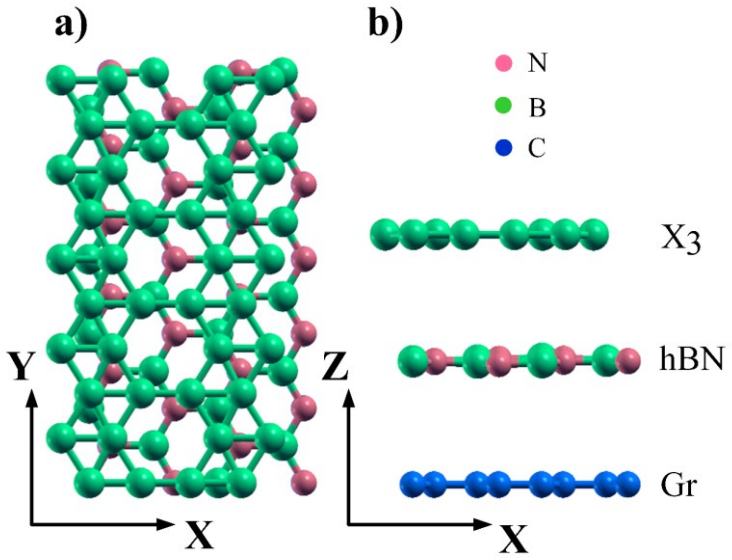

Fig. 3. Schematic showing of relaxed Gr-hBN-χ_3_AA supercell (a) top view and (b) side view. Red, green, and blue spheres show nitrogen, boron, and carbon atoms.

The DFT results in this section are a yardstick for constructing the TB model. In this regard, to find the dominant orbitals, we calculated the partial density of state (PDOS) of the Gr-hBN-χ_3_AA supercell, as shown in Fig. 4. These post-processing calculations are performed by the QE PROJWFC module [29]. Fig. 4(a) illustrates the PDOS of the S, Px, Py, and Pz orbitals of the boron atoms of χ_3 borophene. As we can see, the Py and Pz orbitals of the boron atoms of χ_3 borophene pick up around the Fermi energy level. The PDOS of the orbitals of boron (nitrogen) atoms in hBN are shown in Fig. 4(b) (Fig. 4(c)). The Pz orbitals of boron and nitrogen atoms have the highest DOS contribution around the Fermi level. Like the hBN layer, the Pz orbital of the carbon atoms in Gr has higher DOS around E_F (Fig. 4(d)). Based on these calculations, we have employed these dominant orbitals in the TB model. Finally, Fig. 4(e) shows the PDOS of the S and P orbitals, and also the total PDOS of the whole supercell.

AUT Journal of Electrical Engineering
10.22060/EEJ.2025.23756.5632

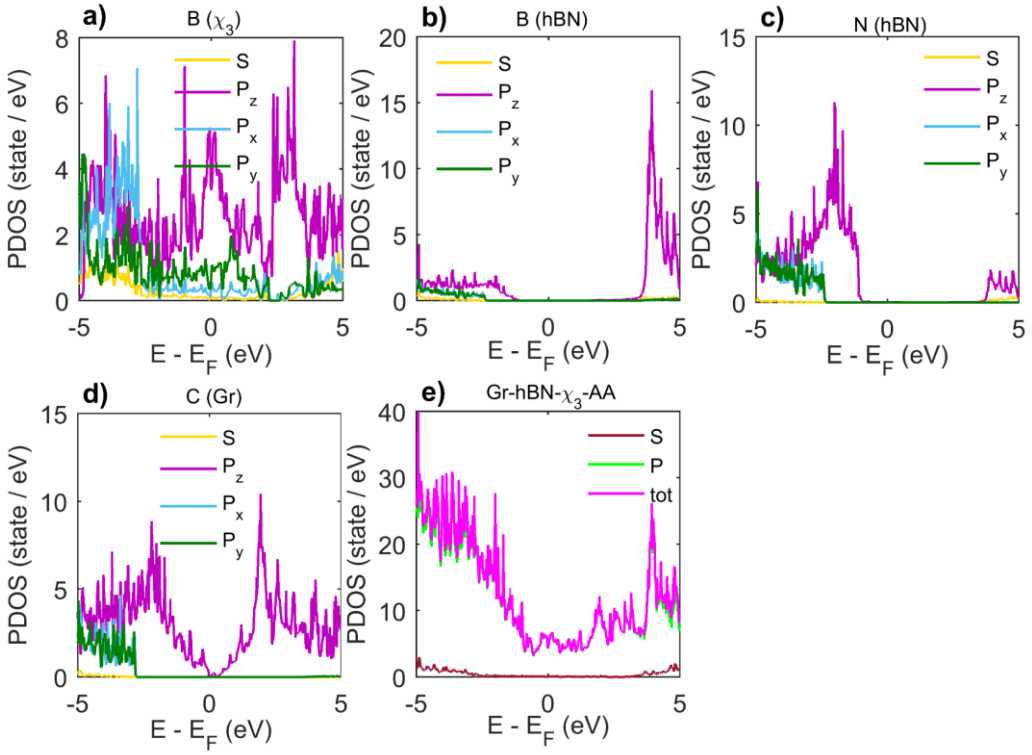

Fig. 4. PDOS for Gr-hBN-χ_3_AA supercell. For orbitals of (a) B atoms in χ_3 borophene, (b) B, (c) N atoms in hBN layer, (d) C atoms in Gr, (e) S, P, and total PDOS of Supercell.

To find the conduction band minimum (ΔE_C) and the valence band maximum (ΔE_V) between Gr and hBN layers, we carried out orbital projection calculations that are shown in Fig. 5. Fig. 5(a) separates bands of the three layers graphene (red), boron nitride (blue), and χ_3 borophene (green) in the Gr-hBN-χ_3_AA supercell. Similarly, Fig. 5(b) shows separate orbitals of the atoms of the three materials involved in the band structure. According to this figure, the most effective orbitals involved in the band structure, at the energy levels close to Fermi energy, are the Pz orbitals of C atoms in graphene, the Pz orbitals of B and N atoms in boron nitride, and the Py and Pz orbitals of B atoms in χ_3 borophene. The point with the * sign on the energy axis is the Dirac point of graphene (0.23 eV). Also, ΔE_C (ΔE_V) between graphene and hBN is 3.26 (1.34) eV.

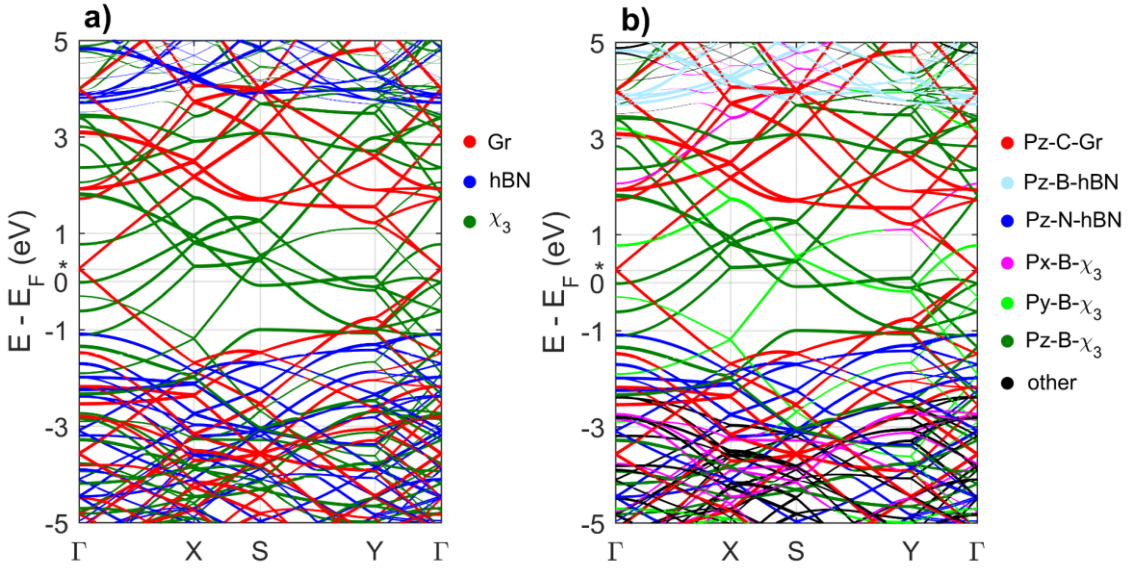

Fig. 5. Projection band structure (PBAND) for Gr-hBN-χ_3_AA supercell. (a) Separate bands for three materials of the structure (b) separate orbitals of atoms of three layers. The * sign on the vertical axis corresponds to the Dirac point energy of graphene, which is 0.23 eV.

Moreover, we calculated the electron concentration function (ELF) to illustrate the chemical bonds of the Gr-hBN-χ_3_AA supercell (Fig. 6). Generally, the ELF value is in the range of 0-1. For $0 < ELF \leq 0.5$, the interatomic bonds are ionic; otherwise, those are considered covalent [30]. Figs. 6(a)-6(c) show the 2D ELF plots for the Gr, hBN and χ_3 borophene layers, respectively. For Gr and hBN layers, each atom creates covalent bonds with its three neighboring atoms. For the χ_3 borophene layer, atoms with 4 (5) neighbors form strong covalent bonds with 3 (2) neighbors. The 2D ELF view of the supercell from the side view is shown in Fig. 6(d) so that vdW bonds between atoms in different layers are evident.

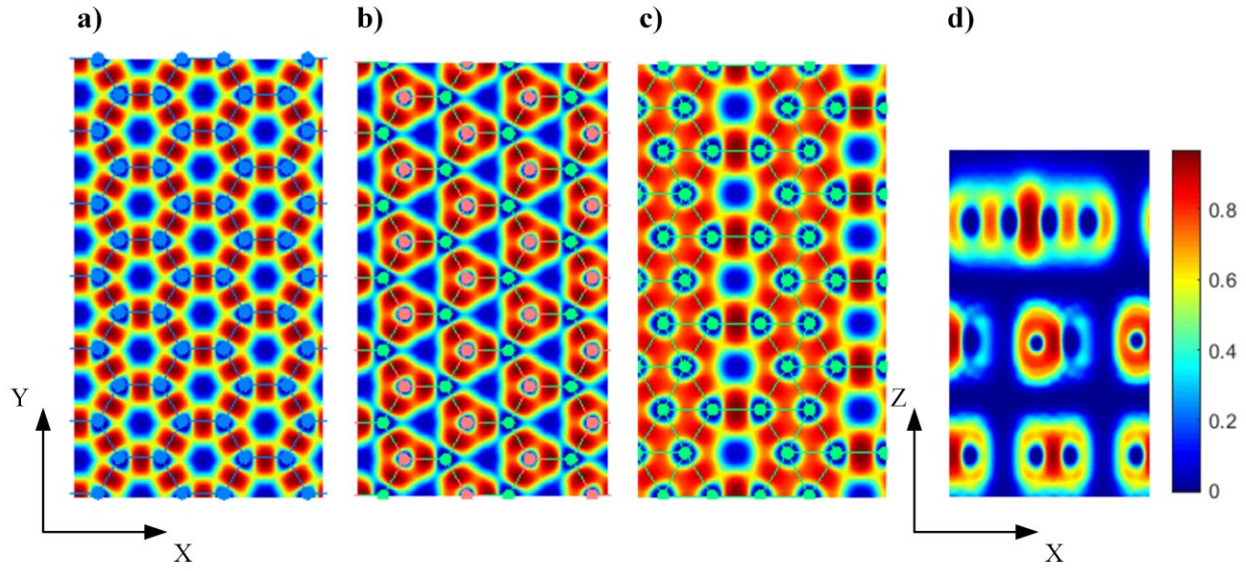

Fig. 6. (a) 2D-ELF profile form (a) bottom view (Gr), (b) hBN, (c) top view (χ_3 borophene). (d) side view of Gr-hBN-χ_3_AA supercell. From the bottom, the first to third layers are graphene, boron nitride, and χ_3 borophene.

B. Tight-Binding Modeling

The TB model is a popular method for calculating the band structure of solid-state systems [31]. Hamiltonian of the studied heterostructure is as follows:

$$[H]=[H_0]+\sum_{m=1}^{4}[H_{nm}]\exp\left(i\vec{k}\vec{d}_m\right) \qquad (1)$$

$[H_0]$ is the unit cell Hamiltonian, and $[H_{nm}]$ is the interaction between the unit cell and the neighbor's mth unit cell. $\vec{d}_m$ defines the vector that connects the unit cell to the mth neighbor. $[H_0]$ in (1) is as follows:

$$[H_0]=\begin{pmatrix} H_{Gr} & \zeta_{Gr-hBN} & \\ \zeta^{\dagger}_{Gr-hBN} & H_{hBN} & \zeta_{hBN-\chi_3} \\ & \zeta^{\dagger}_{hBN-\chi_3} & H_{\chi_3} \end{pmatrix} \qquad (2)$$

10.22060/EEJ.2025.23756.5632

In (2), H_{χ_3} and H_{Gr} are hopping between boron and carbon atoms on the χ_3 and Gr sheets, respectively. H_{hBN} describes a Hamiltonian matrix of the hBN layer. Out-plane hopping between carbon atoms in the graphene layer and boron and nitrogen atoms in the hBN layer is described by ζ_{Gr-hBN}. Similarly, $\zeta_{hBN-\chi_3}$ depicts out-plane hopping between boron and nitrogen atoms in the hBN layer and boron atoms in the χ_3 borophene layer. All relevant hopping parameters are described based on Slater Koster (SK) parameters [31].

To find the out-plane hopping between χ_3 and hBN layers, i.e., $\zeta_{hBN-\chi_3}$, we consider the interlayer hopping of the ith B atom in the χ_3 layer and the jth B or N atom in the hBN layer [32] as

$$h_{Pz(B)/Pz(B)}(i,j)=\left[n_{i,j}^2\left(V_{pp\sigma}^{B,B}\right)+\left(1-n_{i,j}^2\right)\left(V_{pp\pi}^{B,B}\right)\right]\times\exp\left(-\frac{r_{i,j}}{P}\right)^{\xi} \quad (3)$$

$$h_{Pz(B)/Pz(N)}(i,j)=\left[n_{i,j}^2\left(V_{pp\sigma}^{B,N}\right)+\left(1-n_{i,j}^2\right)\left(V_{pp\pi}^{B,N}\right)\right]\times\exp\left(-\frac{r_{i,j}}{P}\right)^{\xi} \quad (4)$$

The cosine of the angle between the vector that points jth B or N atom to ith B atom and the z-axis, represented by $n_{i,j}$. Also, $r_{i,j}$ shows the distance between the ith B atom and the jth B or N atom. ξ and P parameters provide one degree of freedom for a better fit. We consider that the base orbitals are orthonormal; therefore, the overlap matrix is unitary. The SK parameters of the structure are described in Table 1.

Table 1. SK Parameters of device.

Parameters	Onsite	Bond	Layer
$V_{pp\sigma}^{\chi_3}$	…	B-B	χ_3
$V_{pp\pi}^{\chi_3}$	…	B-B	χ_3
$V_{pp\pi}^{hBN}$	…	B-N	hBN
$V_{pp\pi}^{Gr}$	…	C-C	Gr
$V_{pp\sigma}^{B,B}$	…	B-B (vertical)	χ_3 & hBN
$V_{pp\pi}^{B,B}$	…	B-B (vertical)	χ_3 & hBN
$V_{pp\sigma}^{B,N}$	…	B-N (vertical)	χ_3 & hBN
$V_{pp\pi}^{B,N}$	…	B-N (vertical)	χ_3 & hBN
$V_{pp\sigma}^{B,C}$	…	B-C (vertical)	hBN & Gr
$V_{pp\sigma}^{N,C}$	…	N-C (vertical)	hBN & Gr
$\Delta_{p_y}^{\chi_3}$	Py_B	…	χ_3
$\Delta_{p_z}^{\chi_3}$	Pz_B	…	χ_3
$\Delta_{p_z(B)}^{hBN}$	Pz_B	…	hBN
$\Delta_{p_z(N)}^{hBN}$	Pz_N	…	hBN
$\Delta_{p_z}^{Gr}$	Pz_C	…	Gr

10.22060/EEJ.2025.23756.5632

To fit the DFT and TB band structures, we apply the least-squares method [33]. Data of DFT and TB band structures are specified by E_j^{DFT} and E_j^{TB}, which represents the j band at k point. The error function is defined as a weighted sum as follows:

$$S(p)=\sum_j \frac{\left[E_j^{DFT}-E_j^{TB}\right]^2}{\sigma_j^2} \qquad (5)$$

Where σ_j and p are the weight of the error function and TB parameters, respectively. To obtain the optimal SK parameters, function S is minimized with respect to p. The best TB parameters are presented in Table 2. Fig. 7 compares DFT and TB band structures.

Table 2. TB parameters Gr–hBN–χ_3–AA

Parameter	Value	Parameter	Value
$V_{pp\sigma}^{\chi_3}$	3.075 (eV)	$V_{pp\sigma}^{B,B}$	0.1 (eV)
$V_{pp\pi}^{\chi_3}$	-1.65 (eV)	$V_{pp\pi}^{B,B}$	-0.055 (eV)
$\Delta_{p_y}^{\chi_3}$	2.53 (eV)	$V_{pp\sigma}^{B,N}$	0.11 (eV)
$\Delta_{p_z}^{\chi_3}$	1.2 (eV)	$V_{pp\pi}^{B,N}$	-0.04 (eV)
$V_{pp\pi}^{hBN}$	2.58 (eV)	$V_{pp\sigma}^{B,C}$	0.12 (eV)
$\Delta_{p_z(B)}^{hBN}$	3.5124 (eV)	$V_{pp\sigma}^{N,C}$	0.06 (eV)
$\Delta_{p_z(N)}^{hBN}$	-1.0849 (eV)	ξ	0
$V_{pp\pi}^{Gr}$	2.53 (eV)	P	1 (Å)
$\Delta_{p_z}^{Gr}$	0.2517 (eV)		

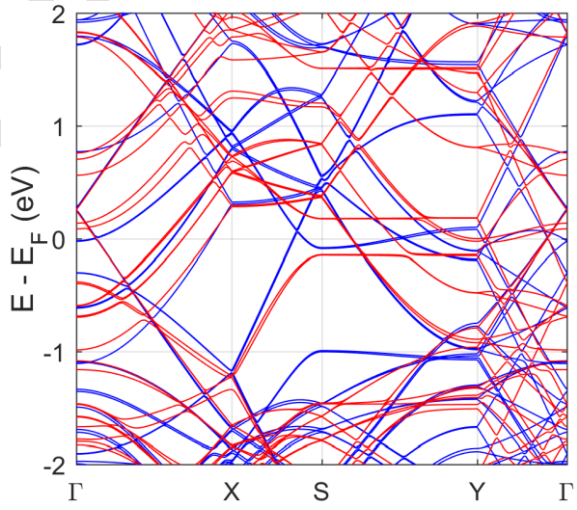

Fig. 7. Comparison of DFT and TB bandstructures

10.22060/EEJ.2025.23756.5632

C. NEGF Technique

Fig. 8(a) and (b) show the side and top views of the device, respectively, in nanoribbon mode (VTGNR χ_3NRFET) and width w=1.477 nm. Also, we have considered the length of the device to be 0.85 nm. The orange color characterizes the channel area. Semi-infinite leads are considered at the ends of the bottom graphene sheet and the top χ_3 borophene sheet, utilizing self-energy definition. This work presents the Hamiltonian in real space mode [34]. In this work, neither the source nor the drain electrodes are doped, and scattering effects have been neglected during calculation.

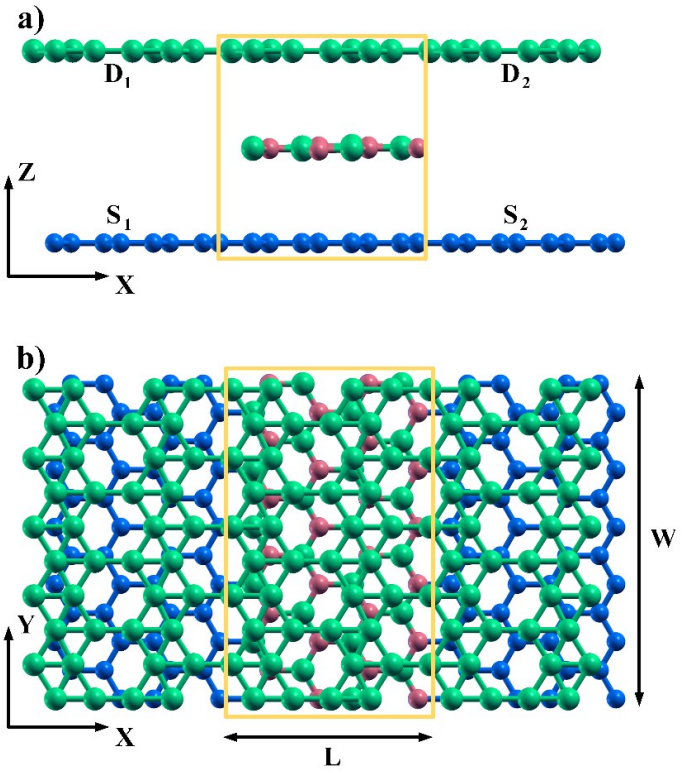

Fig. 8. Schematic of channel, and source and drain contacts of VTGNRχ_3NRFET and width W=1.477 nm (a) Side (b) Top view.

The retarded Green's function with four contacts, the transmission function, current, and total current between j and k contacts of the device, are represented in Eqs. 6, 7, 8, and 9, respectively [35, 36].

$$G(E)=\left[EI-H-\sum_{S_1}(E)-\sum_{S_2}(E)-\sum_{D_1}(E)-\sum_{D_2}(E)\right]^{-1} \quad (6)$$

$$T_{jk}(E)=\sum_{k_y} Trace\left[\Gamma_j(E)G(E)\Gamma_k(E)G^{\dagger}(E)\right] \quad (7)$$

$$I_{jk}=\frac{2q}{h}\int T_{jk}(E)\left(f_j(E)-f_k(E)\right)dE \quad (8)$$

$$I=\sum_{j,k} I_{j,k} \quad (9)$$

10.22060/EEJ.2025.23756.5632

Where $\sum_{S_1,S_2}$ and $\sum_{D_1,D_2}$ are self-energies of the source and drain contacts, so that j = S_1, S_2 and k = D_1, D_2 and $\Gamma(E)=i\left[\sum(E)-\sum(E)^{\dagger}\right]$ is the broadening function.

Fig. 9 shows the equivalent capacitive circuit model for the device. This model has been used to calculate the potential of barrier layers. C_{OX} and C_t are the gate oxide (SiO_2) and the tunneling barrier (hBN) capacitors, respectively. These two capacitors are calculated by Eq. 10, where t_{ox} and t_{hBN} are the thickness of SiO_2 and hBN, respectively. C_{QS} (C_{QD}) is the quantum capacitor of graphene (borophene) sheets, which is calculated using Eq. 11 [37]. We assumed E_{FS} = 0, and the Fermi level of the drain is $E_{FD} = E_{FS} - qV_B$. The energies of the source and drain Dirac points are $-qVS$ and $-qVD$, respectively. Also, it is assumed that the potential along the hBN layers changes linearly. To calculate the channel potential, the capacitive circuit model of Fig. 9 should be analyzed self-consistent with (11).

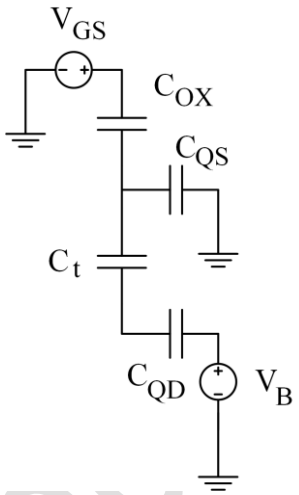

Fig. 9. Equivalent capacitive circuit model for the device.

$$C_{ox}=\varepsilon_{ox}/t_{ox},\quad C_t=\varepsilon_{hBN}/t_{hBN} \qquad (10)$$

$$C_Q(V_{ch})=q^2\int_{-\infty}^{\infty}DOS(E)\frac{\operatorname{sech}^2(E-qV_{ch}/2KT)}{4KT}dE \qquad (11)$$

4. Results

As shown in Fig. 8, the hBN layer has been sandwiched between graphene and χ_3 borophene in the device, with four contacts. In 2D mode, the width of the nanoribbon is also repeated with period W in the Y direction. In calculations, t_{ox} is assumed to be 1nm.

Fig. 10(a) illustrates the transmission coefficient in terms of energy for the device and three different widths. According to the figure, as the width of the nanoribbon decreases, the energy gap (Eg) of the graphene nanoribbon (GNR) increases. Therefore, the transmission coefficient of the carrier decreases. The steep slope of the transmission coefficient around the Dirac point energy of graphene (0.23 eV) indicates the Eg of graphene. Also, for the width of 1.477 nm, it can be seen that the edge of the hBN conduction band is at the energy of 3.49 eV, and the edge of the hBN valence band is at the energy of -1.11 eV. For energies larger

10.22060/EEJ.2025.23756.5632
than the conduction band edge and lower than the valence band edge, the transmission probability is due to thermionic emission.

Fig. 10(b) illustrates the current density of VTGNRχ_3NRFET at a width of 1.477 nm in terms of drain-source voltage for different gate-source voltages. As can be seen, in a $V_{DS} > 0$, the current is low (high) at V_{GS} ($-V_{GS}$), and the transistor is in the OFF (ON) state.

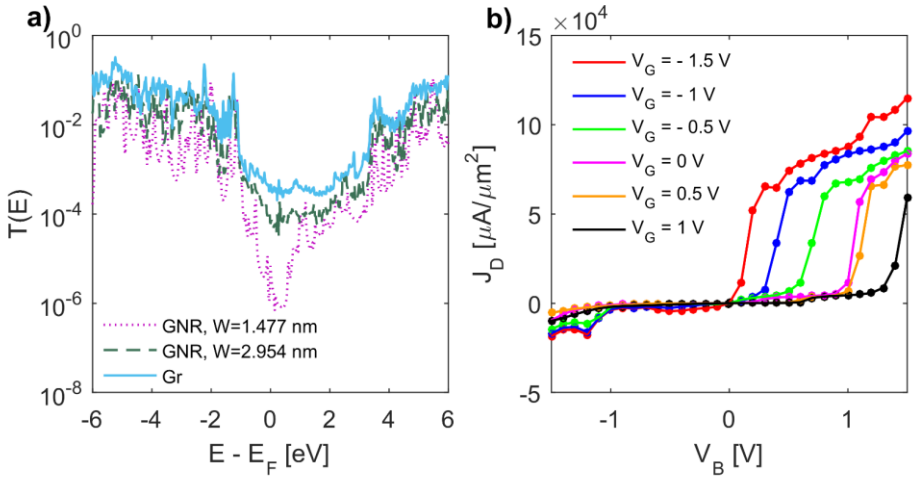

Fig. 10. (a) Transmission coefficient of VTGNRχ_3NRFET for different nanoribbons widths compared to VTGrχ_3FET (b) Drain current density in terms of drain-source voltage for VTGNRχ_3NRFET width W = 1.477 nm.

Switching ratio (I_{ON}/I_{OFF}), subthreshold swing (SS) [34], and gate-delay time (τ) [38] are important characteristics of the device defined as:

$$SS = \frac{dV_G}{d\left(\log\left(I_D\right)\right)} \qquad (12)$$

$$\tau = \frac{Q_{ON} - Q_{OFF}}{I_{ON}} \qquad (13)$$

$$Q = -e\int LDOS\left(E\right)f\left(E - E_F\right)dE + e\int LDOS\left(E\right)f\left(1 - f\left(E - E_F\right)\right)dE \qquad (14)$$

Where Q_{ON} and Q_{OFF} are the total charges of the device in the source and drain regions, at ON and OFF states, respectively, and, LDOS is the local density of states [34].

Table 3. FOM of VTGrχ_3FETs.

Device	I_{ON}/I_{OFF}	SS_{min} (mv/dec)	τ (ps)	$\|V_{DS}\|$	$\|V_{GS}\|$
VTGNRχ_3 NRFET, W=1.477 nm	186	256	0.011	0.5	1.5
VTGNRχ_3 NRFET, W=2.954 nm	3.14	1115	0.5	0.5	1.5
VTGrχ_3FET, 2D	3.12	2014	2.858	0.5	1.5

10.22060/EEJ.2025.23756.5632
Table 3 shows the figure of merit (FOM) of VTGrχ_3FET. As can be seen from the Table 3, the I_{ON}/I_{OFF} ratio of the transistor increases with the decrease in the width of the GNR. Because with the decrease in the width of GNR, the Eg of GNR increases, and as a result, the OFF current decreases, therefore I_{ON}/I_{OFF} increases. Also, the decrease in the ribbon's width improves *SS*. Because it leads to weaker quantum effects (decreasing density of state and quantum capacitances), and it makes the control of the gate on the channel better. Moreover, τ improves with decreasing the width of GNR.

Table 4. Comparison of parameters of considered device with other related works.

References	Structure	$t_{barrier}$ (nm)	SS_{min} (mv/dec)	(I_{ON}/I_{OFF}) max
Brittenl et al. [11]	Gr-hBN-Gr	…	…	50
Yu et al. [16]	Gr-MoS_2-Ti	~15	…	10^3
Liu et al. [18]	Gr-MoS_2-Ag	0.65	…	26
Abbasi et al. [19]	GNR-hBN-χ_3_AB	0.829	343	113
This work	GNR-hBN-χ_3_AA	0.824	256	186

Table 4 compares the parameters of the considered device and other related works (metallic drain). As can be seen from Table 4, the thickness of the tunneling barrier plays an essential role in improving the I_{ON}/I_{OFF}. Also, changing the stack type between Gr and hBN layers has little effect on the FOM of the device [19]. To improve the performance of VTFET, it is recommended to use materials in the source and drain with an energy gap and also in the tunneling barrier with a smaller energy gap [39]. Moreover, a combination of lateral and vertical structure have the potential to improve the performance of VTFET.

5. Conclusion

This work uses DFT theory to investigate the electronic properties (PDOS, PBAND, and ELF) of Gr-hBN-χ_3_AA vertical heterostructure. We concluded that the Gr-hBN-χ_3_AA is less stable than Gr-hBN-χ_3_AB. Also, the NEGF technique, along with the TB model, has been applied to calculate the electrical characteristics of the considered device. The results show that decreasing the width of the device improves parameters I_{ON}/I_{OFF}, *SS*, and τ. The device permits a gate-delay time of 0.011 ps at room temperature. The results show that changing the stack between Gr and hBN layers has little effect on the device's FOM. Also, a combination of lateral and vertical structures with a suitable design can improve the performance of VTFET.

Funding
This research received no funding.

Data availability
All data that support the findings of this study are included in the article.

Conflict of Interest
The authors declare that they have no conflict of interest.

References

[1] E.G. Marin, M. Perucchini, D. Marian, G. Iannaccone, G. Fiori, Modeling of Electron Devices Based on 2-D Materials, IEEE Transactions on Electron Devices, 65(10) (2018) 4167-4179.

[2] J. Yan, Z.X. Shen, Electronic Devices Based on Transition Metal Dichalcogenides, in: N.S. Arul, V.D. Nithya (Eds.), Springer Singapore, Singapore, 2019, pp. 331-355.

[3] B. Zhao, D. Shen, Z. Zhang, P. Lu, M. Hossain, J. Li, B. Li, X. Duan, 2D Metallic Transition-Metal Dichalcogenides: Structures, Synthesis, Properties, and Applications, Advanced Functional Materials, 31(48) (2021) 2105132-2105132.

[4] G. Iannaccone, F. Bonaccorso, L. Colombo, G. Fiori, Quantum engineering of transistors based on 2D materials heterostructures, Nature Nanotechnology, 13(3) (2018) 183-191.

[5] I.C. Cherik, S. Mohammadi, P.K. Hurley, L. Ansari, F. Gity, Investigating vertical charge plasma tunnel field effect transistors beyond semiclassical assumptions, Scientific Reports, 15(1) (2025) 4682.

[6] X. Yang, R. He, Z. Lu, Y. Chen, L. Liu, D. Lu, L. Ma, Q. Tao, L. Kong, Z. Xiao, S. Liu, Z. Li, S. Ding, X. Liu, Y. Li, Y. Wang, L. Liao, Y. Liu, Large-scale sub-5-nm vertical transistors by van der Waals integration, Nature Communications, 15(1) (2024) 7676.

[7] L. Merces, L.M.M. Ferro, A. Nawaz, P. Sonar, Advanced Neuromorphic Applications Enabled by Synaptic Ion-Gating Vertical Transistors, Advanced Science, 11(27) (2024) 2305611.

[8] Z. Mei, X. Li, L. Liang, Y. Li, Z. Zhao, Z. Zhou, Q. Li, S. Fan, J. Wang, Y. Wei, Two-Dimensional Vertical Transistor with One-Dimensional van der Waals Contact, ACS Nano, 18(41) (2024) 28301-28310.

[9] Y. Lv, W. Qin, C. Wang, L. Liao, X. Liu, Recent Advances in Low-Dimensional Heterojunction-Based Tunnel Field Effect Transistors, Advanced Electronic Materials, 5(1) (2019) 1800569-1800569.

[10] VTFET, in, 2021, https://uk.pcmag.com/processors/137687/ibm-samsung-tout-new-vertical-transistor-for-future-computer-chips.

[11] L. Britnell, R.V. Gorbachev, R. Jalil, B.D. Belle, F. Schedin, A. Mishchenko, T. Georgiou, M.I. Katsnelson, L. Eaves, S.V. Morozov, N.M.R. Peres, J. Leist, A.K. Geim, K.S. Novoselov, L.A. Ponomarenko, Field-effect tunneling transistor based on vertical graphene heterostructures, Science, 335(6071) (2012) 947-950.

[12] M. Ebrahimi, A. Horri, M. Sanaeepur, M.B. Tavakoli, A comparative computational study of tunneling transistors based on vertical graphene-hBCN heterostructures, Journal of Applied Physics, 127(8) (2020) 084504-084504.

[13] A. Horri, R. Faez, M. Pourfath, G. Darvish, Modeling of a Vertical Tunneling Transistor Based on Graphene-MoS2 Heterostructure, IEEE Transactions on Electron Devices, 64(8) (2017) 3459-3465.

[14] J. Park, T.W. Kim, G.H. Oh, J.G. An, S.I. Kim, J.C. Shin, Ultralow Subthreshold Swing 2D/2D Heterostructure Tunneling Field-Effect Transistor with Ion-Gel Gate Dielectrics, ACS Applied Electronic Materials, 5(1) (2023) 196-204.

[15] D. Sarkar, X. Xie, W. Liu, W. Cao, J. Kang, Y. Gong, S. Kraemer, P.M. Ajayan, K. Banerjee, A subthermionic tunnel field-effect transistor with an atomically thin channel, Nature, 526(7571) (2015) 91-95.

[16] W.J. Yu, Z. Li, H. Zhou, Y. Chen, Y. Wang, Y. Huang, X. Duan, Vertically stacked multi-heterostructures of layered materials for logic transistors and complementary inverters, Nature Materials, 12(3) (2013) 246-252.

[17] J.H. Lee, D.H. Shin, H. Yang, N.B. Jeong, D.H. Park, K. Watanabe, T. Taniguchi, E. Kim, S.W. Lee, S.H. Jhang, B.H. Park, Y. Kuk, H.J. Chung, Semiconductor-less vertical transistor with I ON/I OFF of 106, Nature Communications, 12(1) (2021) 1-8.

[18] L. Liu, L. Kong, Q. Li, C. He, L. Ren, Q. Tao, X. Yang, J. Lin, B. Zhao, Z. Li, Y. Chen, W. Li, W. Song, Z. Lu, G. Li, S. Li, X. Duan, A. Pan, L. Liao, Y. Liu, Transferred van der Waals metal electrodes for sub-1-nm MoS2 vertical transistors, Nature Electronics, 4(5) (2021) 342-347.

[19] R. Abbasi, R. Faez, A. Horri, M.K. Moravvej-Farshi, Modeling of a vertical tunneling transistor based on Gr-hBN- χ 3borophene heterostructure, Journal of Applied Physics, 132(3) (2022) 034302-034302.

[20] F. Wu, H. Tian, Y. Shen, Z. Hou, J. Ren, G. Gou, Y. Sun, Y. Yang, T.L. Ren, Vertical MoS2 transistors with sub-1-nm gate lengths, Nature, 603(7900) (2022) 259-264.
[21] A.J. Mannix, X.F. Zhou, B. Kiraly, J.D. Wood, D. Alducin, B.D. Myers, X. Liu, B.L. Fisher, U. Santiago, J.R. Guest, M.J. Yacaman, A. Ponce, A.R. Oganov, M.C. Hersam, N.P. Guisinger, Synthesis of borophenes: Anisotropic, two-dimensional boron polymorphs, Science, 350(6267) (2015) 1513-1516.

[22] B. Feng, J. Zhang, Q. Zhong, W. Li, S. Li, H. Li, P. Cheng, S. Meng, L. Chen, K. Wu, Experimental realization of two-dimensional boron sheets, Nature Chemistry, 8(6) (2016) 563-568.

[23] M. Ou, X. Wang, L. Yu, C. Liu, W. Tao, X. Ji, L. Mei, The Emergence and Evolution of Borophene, Advanced Science, 8(12) (2021) 2001801-2001801.

[24] D. Li, J. Gao, P. Cheng, J. He, Y. Yin, Y. Hu, L. Chen, Y. Cheng, J. Zhao, 2D Boron Sheets: Structure, Growth, and Electronic and Thermal Transport Properties, Advanced Functional Materials, 30(8) (2020) 1-32.

[25] G.J. Adekoya, O.C. Adekoya, M. Muloiwa, E.R. Sadiku, W.K. Kupolati, Y. Hamam, Advances In Borophene: Synthesis, Tunable Properties, and Energy Storage Applications, Small, 20(40) (2024) 2403656.

[26] R.K. Mishra, J. Sarkar, K. Verma, I. Chianella, S. Goel, H.Y. Nezhad, Borophene: A 2D wonder shaping the future of nanotechnology and materials science, Nano Materials Science, 7(2) (2025) 198-230.

[27] Y. Park, Y. Wang, V. Gladkikh, D. Hedman, X. Kong, F. Ding, High temperature phases of borophene: borophene glass and liquid, Nanoscale Horizons, 8(3) (2023) 353-360.

[28] R. Abbasi, R. Faez, A. Horri, M.K. Moravvej-Farshi, Tight-Binding Model of χ 3 and β 12 Structures of Borophene, Journal of Electronic Materials, 52(4) (2023) 2544-2552.

[29] P. Giannozzi, S. Baroni, N. Bonini, M. Calandra, R. Car, C. Cavazzoni, D. Ceresoli, G.L. Chiarotti, M. Cococcioni, I. Dabo, A. Dal Corso, S. De Gironcoli, S. Fabris, G. Fratesi, R. Gebauer, U. Gerstmann, C. Gougoussis, A. Kokalj, M. Lazzeri, L. Martin-Samos, N. Marzari, F. Mauri, R. Mazzarello, S. Paolini, A. Pasquarello, L. Paulatto, C. Sbraccia, S. Scandolo, G. Sclauzero, A.P. Seitsonen, A. Smogunov, P. Umari, R.M. Wentzcovitch, QUANTUM ESPRESSO: A modular and open-source software project for quantum simulations of materials, Journal of Physics Condensed Matter, 21(39) (2009).

[30] B. Silvi, A. Savin, Classification of chemical bonds based on topological analysis of electron localization functions, in, 1994, pp. 683-686.

[31] J.C. Slater, G.F. Koster, Simplified LCAO method for the periodic potential problem, Physical Review, 94(6) (1954) 1498-1524.

[32] S. Fang, R. Kuate Defo, S.N. Shirodkar, S. Lieu, G.A. Tritsaris, E. Kaxiras, Ab initio tight-binding Hamiltonian for transition metal dichalcogenides, Physical Review B - Condensed Matter and Materials Physics, 92(20) (2015) 1-15.

[33] R. Fletcher, M.J.D. Powell, A Rapidly Convergent Descent Method for Minimization, The Computer Journal, 6(2) (1963) 163-168.

[34] M.P. Anantram, M.S. Lundstrom, D.E. Nikonov, Modeling of nanoscale devices, Proceedings of the IEEE, 96(9) (2008) 1511-1550.

[35] S. Datta, Quantum transport: Atom to transistor, 2005.

[36] M. Pourfath, Green's Function Formalism, in: M. Pourfath (Ed.), Springer Vienna, Vienna, 2014, pp. 105-156.

[37] H. Kolavada, S. Singh, I. Lukačević, P.N. Gajjar, S.K. Gupta, Quantum capacitance of multi-layered δ-6 borophene: A DFT study, Electrochimica Acta, 439 (2023) 141589-141589.

[38] J. Guo, A. Javey, H. Dai, M. Lundstrom, Performance analysis and design optimization of near ballistic carbon nanotube field-effect transistors, in, pp. 703-706.

[39] R. Abbasi, R. Faez, A. Horri, M.K. Moravvej-Farshi, Numerical Study of a Vertical Tunneling Transistor Based on Gr/BC2N/BC6N and BC2N′/hBN/BC2N′ Heterostructures, ACS Applied Electronic Materials, 5(7) (2023) 3612-3624.